

1 Spatial influence of agricultural residue burning and aerosols on land surface
2 temperature

3 Akanksha Pandey¹, Richa Singh¹, Kumari Aditi^{1,2}, Neha Chhillar¹, Tirthankar Banerjee^{1,2*}

4

5 ¹ Institute of Environment and Sustainable Development, Banaras Hindu University, Varanasi, India.

6 ²DST-Mahamana Centre of Excellence in Climate Change Research, Banaras Hindu University, Varanasi, India.

7 *Correspondence to: T. Banerjee (tb.iesd@bhu.ac.in; tirthankaronline@gmail.com)

8

9 Abstract

10 The biophysical effects of agricultural residue burning, driven by the excessive release of
11 energy and carbonaceous aerosols, remain poorly quantified at the global scale. Residue-
12 based fires have the potential to modify regional climate by altering land surface temperature
13 (LST), highlighting the need for investigation at regional scale. Here, an observation-driven
14 assessment of spatial variations in LST due to concurrent release of energy and aerosols has
15 been made over northwestern India using multiple satellite and reanalysis-based datasets.
16 Year-specific fire pixel density was used to delineate an intensive fire zone characterized by
17 medium-to-large residue-based fire. Geospatial analysis revealed positive association among
18 FRP (fire radiative power), LST and AOD (aerosol optical depth). Over intensive fire zone, a
19 space-for-time approach revealed significant increase in both Δ LST (0.57°C; 95% CI:0.33-
20 0.81°C) and Δ AOD (0.13; 95% CI:0.08–0.17) due to fire. Random Forest non-linear model was
21 employed to regress potential influence of FRP and AOD on LST having several other variables
22 as confounding factors. FRP consistently emerged as the dominant predictor of LST, followed
23 by planetary boundary layer height and aerosols. An increase in relative feature importance
24 of FRP was noted during days having high fire intensity and positive association with LST.
25 Geographically weighted regression further explained spatial heterogeneity in LST
26 modulation by FRP. Overall, this analysis provides the first empirical evidence that residue-
27 based fire contributes to changes in land surface temperature. It further highlights that the
28 magnitude of this perturbation is governed by interannual variations in fire intensity and
29 influenced strongly by prevailing meteorological conditions.

30 **Keywords:** Aerosols, Biomass burning, Fire, GWR, Random Forest.

31

32

33

34 **Introduction**

35 Burning agricultural residues is a widespread practice for the rapid removal of post-
36 harvest biomass from croplands in many regions of the world (Streets et al., 2003; Singh et
37 al., 2018; Shyamsundar et al., 2019). While biomass burning is often associated with
38 deforestation (Chuvieco et al., 2021), forest fires (van der Velde et al., 2021; Aditi et al., 2025),
39 and shifting cultivation (Prasad et al., 2000), residue burning on agricultural land is primarily
40 conducted to clear fields, fertilize soil, eradicate weeds and pests, and prepare land for the
41 next crop cycle (Graham et al., 2002; Korontzi et al., 2006; Lan et al., 2022). This practice is
42 observed across large agricultural regions globally, including China (Streets et al., 2003; Zhang
43 et al., 2020), South America (Graham et al., 2002), Southeast Asia (Lasko and Vadrevu, 2018;
44 Yin, 2020), and northwestern India (Singh et al., 2018, 2021; Sarkar et al., 2018). In
45 northwestern India, extensive residue burning during October to November is a recurring
46 phenomenon and has been widely examined from multiple perspectives. Previous studies
47 report that these burning events contribute to severe air-quality degradation in downwind
48 urban centers (Singh et al., 2018; Jethva et al., 2019), alter aerosol loading and chemistry
49 (Mhawish et al., 2022), modify aerosol vertical stratification and radiative forcing (Hsu et al.,
50 2003; Vinjamuri et al., 2020; Banerjee et al., 2021), induce adverse health effects (Singh et al.,
51 2021), and may influence regional hydrological processes (Kant et al., 2023). However, limited
52 attention has been paid to investigate its effect on urban climate, especially on modulating
53 lower atmospheric thermal budget which has been otherwise strongly evident in case of
54 forest fire (Liu et al., 2018, 2019).

55 Across the northwestern India, dual cropping pattern including rice and wheat crop is
56 predominately practised over roughly 4.1 million ha of land (NAAS, 2017). Such a cropping
57 pattern leads to generation of huge crop residues that are low in nutrient content and rich in
58 silica and ash. Typically, residues from rice-wheat cropping system possess limited economic
59 value, as they are unsuitable for use as alternative fodder, bioenergy feedstock or as raw
60 material in pulp and paper industry (Shyamsundar et al., 2019; Lan et al., 2022). Besides, with
61 the introduction of mechanical harvester in the 1980s and enactment of groundwater
62 preservation act in the late 2000s, in situ burning of agricultural residues has become a
63 recurrent practice among the local farmers. This practice serves to expedite field clearance
64 and reduce the turnaround period between rice harvest and the subsequent sowing of the

65 wheat crop (Balwinder-Singh et al., 2019). India produces an estimated 500 million metric
66 tonnes (MT) of crop residues annually, of which 20–25% are disposed of through open-field
67 burning. Crop residue burning is particularly prevalent in northwestern India, where roughly
68 20-25 MT of residues are set on fire each year (Balwinder-Singh et al., 2019; Lan et al., 2022).
69 Unregulated residue burning in this region contributes approximately 300 Gg/yr of PM_{2.5} and
70 50 Tg of CO₂ equivalent green-house gas emission (Singh et al., 2020). Notably, the frequency
71 of fire incidences has exhibited a persistent upward trend, coinciding with concurrent
72 increases in vegetation indices and atmospheric aerosol loading (Vadrevu et al., 2019; Jethva
73 et al., 2019). In addition to atmospheric emissions, fires exert numerous biophysical impacts
74 on the surrounding ecosystems. Fire induces a cascade of consequential processes, including
75 modifications to the surface energy balance, redistribution of nutrients, alterations in species
76 composition, changes in surface albedo, and variations in evapotranspiration rate (Ward et
77 al., 2012; Liu et al., 2019). Additionally, fire can induce certain biogeochemical and biophysical
78 stresses on local environment by modifying atmospheric composition and surface properties
79 (Andela et al., 2017; Aditi et al., 2025). Such transformation of the native landscape, coupled
80 with excessive release of energy, aerosols and its precursors, may therefore have several
81 potential implications on the environment.

82 Most studies on biomass-based fires have focused on identifying land–atmosphere
83 processes responsible for fire initiation and propagation, quantifying emissions, and
84 evaluating fire-induced land–atmosphere exchanges (Lasko and Vadrevu, 2018; Jethva et al.,
85 2019; Chuvieco et al., 2021; Aditi et al., 2025). In contrast, there is a paucity of knowledge
86 regarding how biomass burning contributes to climate feedbacks through modifications of
87 Earth’s surface radiative budget and land surface temperature (Bowman et al., 2009; Andela
88 et al., 2017). Plausible explanation to this includes limited observation and associated
89 uncertainties in estimating key biophysical parameter like surface albedo, land-atmosphere
90 exchange of sensible heat flux and water vapor, changes in evapotranspiration before and
91 after fire events. There are instances when global forest fire incidences and size have been
92 linked with modifications in land surface temperature (LST; Alkama and Cescatti, 2016; Liu et
93 al., 2018, 2019). Likewise, Liu et al. (2019) noted an enhancement in mean annual LST over
94 burned forest area in the northern high latitudes. Similar evidence of increase in summertime
95 surface radiometric temperature over temperate and boreal forests in the Northern

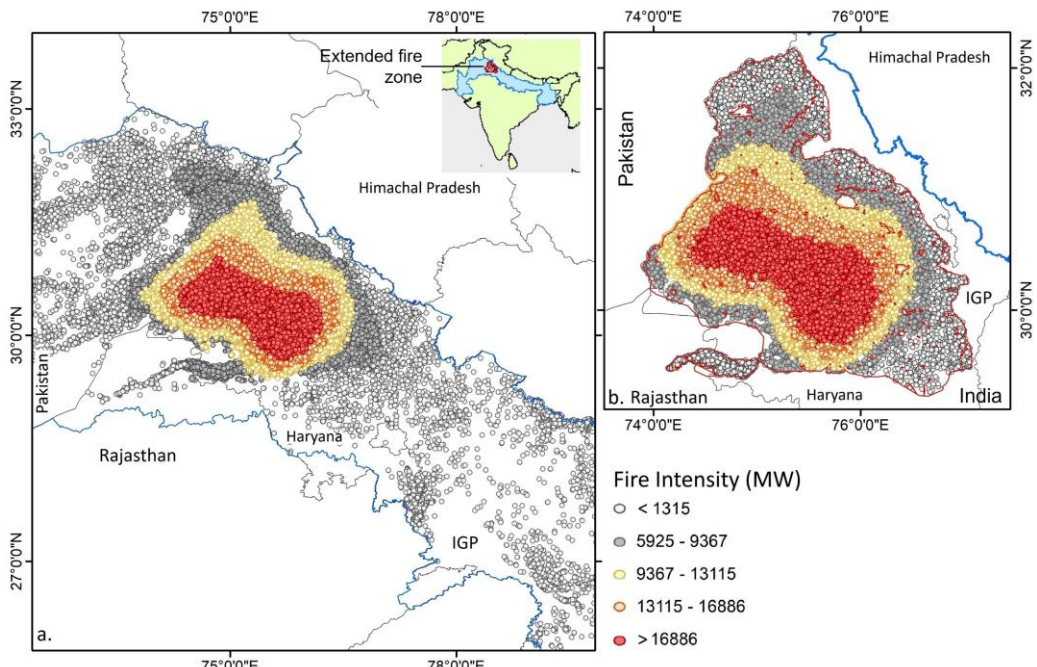
96 Hemisphere was accounted by Zhao *et al.* (2024). Alkama and Cescatti (2016) reported
97 increases in mean and maximum air temperature over arid regions following forest loss,
98 highlighting the sensitivity of surface temperature to land-cover modification. However, fire-
99 induced thermal forcing is strongly constrained by the fire size (Zhao *et al.*, 2024). Small, short-
100 lived fires, such as those associated with agricultural residue burning, often fail to produce
101 sufficiently large changes in surface albedo or evapotranspiration, and therefore may not
102 generate a detectable LST response. Incidence of elevated LST over different provinces in
103 China due to agricultural residue burning has only recently reported by Zhang *et al.* (2020). A
104 spatially heterogeneous increase in LST correlated strongly with fire count, with highest LST
105 gradient noted at distances of 4–10 km from the central point of crop residue burning and
106 persisting for 1–3 days. In contrast, the effects of post-harvest fire incidences in northwestern
107 India on LST remain largely unexplored. This gap introduces considerable uncertainty in
108 assessing the climate feedback of crop residue burning and highlights the need for a better
109 understanding of the underlying mechanisms.

110 This study aims to explore immediate biophysical effect of agricultural residue fire on
111 surface temperature over northwestern India. By integrating spatially and temporally
112 consistent satellite observations and reanalysis datasets, including fire counts, fire radiative
113 power, land surface temperature, aerosols, meteorological covariates, topography, surface
114 property, and physical environment over intensive fire zone, we sought to quantify time-
115 bound changes in LST in response to variations in fire intensity and aerosol loading. Several
116 statistical methods were applied to construct the changes in LST with fire severity and
117 aerosols. Additionally, a space-for-time framework was followed to assess the effects of
118 recurrent FRP variations on LST and aerosol optical depth (AOD) throughout the fire season.
119 Specifically, we addressed two key questions: (1) Does LST respond to changes in fire intensity
120 over northwestern India? and (2) How do local meteorology and aerosol loading modulate
121 LST variation with respect to space and time? To the best of our knowledge, this is the first
122 systematic assessment of agricultural residue fire–driven modulations in LST over
123 northwestern India. By integrating multiple geospatial observations, the analysis offers critical
124 insights into the biophysical feedbacks of residue-based fire and advances understanding of
125 LST responses to residue burning. Further, it refines estimates of fire-induced perturbations

126 in the regional radiative budget offering valuable representation of biomass-based fire in
127 Earth system models.

128 **2. Dataset and methodology**

129 **2.1 Study domain**



130
131 Fig. 1. Spatial variation in satellite-based fire radiative power across northwest India,
132 distribution of FRP-based fire intensity (MW/pixel) (a) and domain selected for
133 retrieval and processing of SNPP VIIRS FRP, AOD and Aqua MODIS LST (b). The region
134 marked with blue in Fig. 1a subset indicates the Indo-Gangetic Plain (IGP) spanning
135 from Pakistan to Bangladesh through India. The extended fire zone selected for
136 analysis is marked with red within the IGP and has been shown in detail in Fig. 1a with
137 fire pixel density. India shape file is acquired from Survey of India archive.

138
139 Post-harvest biomass burning is predominantly practiced across the northwestern
140 Indo-Gangetic Plain (IGP) of South Asia, particularly in the agrarian states of Punjab and
141 Haryana, which together contribute nearly 60–70% of India's total food grain production. The
142 concurrent rise in rice and wheat cultivation has led to a substantial increase in crop residue
143 generation, resulting in higher fire intensity in recent years (Jethva et al., 2019). In this study,
144 geospatial analyses of LST, fire activity, and aerosol loading were conducted over
145 northwestern India during October–November between 2017 and 2021. The combination of

146 high agricultural output, extensive biomass burning, and increasing fire activity makes this
147 region particularly suitable for investigating fire dynamics and their environmental
148 implications. Instead of defining a fixed spatial domain a priori, year-wise fire signals were
149 retrieved across cropland areas in northwestern India. This approach allowed the delineation
150 of a core study region that varied annually according to year-specific fire intensity and spatial
151 trends (as shown in Fig. S2), but all eventually bound to 29.2770° to 32.1625° N and 73.8996°
152 to 77.0718° E, as illustrated in Fig. 1b.

153 **2.2 Spatial dataset**

154 Active fire count data was retrieved from the standard fire product of Visible Infrared
155 Imaging Radiometer Suite (VIIRS) Collection-2 (VNP14IMG) available at 6-min L2 swath at 375
156 m resolution. The VIIRS onboard the Suomi National Polar-orbiting Partnership (SNPP) satellite
157 is a cross-track single-angle scanning radiometer which was launched in year 2011 under joint
158 operation of NASA and NOAA. The VIIRS fire detection algorithm typically extends well refined
159 and validated MODIS Fire and Thermal Anomalies product (Giglio et al., 2003). The I-band
160 based fire detection algorithm primarily utilizes brightness temperature of Channel I4 on
161 middle infrared spanning from 3.55 to 3.93 μm , centred at 3.74 μm . Additionally, to isolate
162 the active fire spots from the fire-free background channel, a single gain I5 at thermal infrared
163 regions (10.5–12.4 μm) is also considered. Rest of the I-band channels i.e. I1 to I3, covering
164 visible, near and short-wave IR are used to distinguish pixels with cloud, water and sun-glint
165 (Schroeder et al., 2014). The VIIRS fire database was considered due to its superior precision
166 and accuracy in identifying relatively small fire, greater spatial resolution at footprint and pixel
167 saturation temperature (Li et al., 2018; Vadrevu and Lasko, 2018; Aditi et al., 2023). For this
168 experiment, SNPP VIIRS 375 m L2 active fire count data with nominal (fire mask class 8) and
169 high confidence (fire mask class 9), was retrieved over northwestern India from year 2017 to
170 2021 (all inclusive).

171 Fire radiative power (FRP) quantifies the release of radiative energy from biomass
172 burning integrated at all angles and wavelengths over a spatial scale. Measured in Watt, FRP
173 retrieval quantifies the release of heat energy against time and in many instances linearly
174 associated with the rate of fuel consumption and emission (Ichoku et al., 2008; Nguyen and
175 Wooster, 2020). A detailed description on FRP retrieval and comparison among the sensors
176 are available in Wooster et al. (2003, 2005) and Ichoku et al. (2008). Li et al. (2018) concluded

177 VIIRS FRP as comparable with MODIS FRP in most of fire clusters and stable across swath.
178 Here, FRP (MW) was processed from the SNPP VIIRS C2 Level-2 (L2) 375 m active fire product
179 (VNP14IMG). VIIRS FRP was used as a proxy of fire intensity and potential emission strength
180 from the biomass burning area, and considered as a direct measurement of radiative energy
181 being released from individual fire pixel.

182 Land surface temperature (LST, in °C) at 1 km spatial resolution was utilized from
183 Moderate Resolution Imaging Spectroradiometer (MODIS) version 6.1 Land Surface
184 Temperature and Emissivity retrievals product (MYD11A1). Typically, LST indicates
185 thermodynamic temperature of the interface atmospheric layer within soil, plant cover and
186 lower atmosphere, and serves as an indicator of land-atmosphere interaction and exchange
187 (Li et al., 2023). Here, MODIS MYD11A1 radiometric dataset with quality flag '00' was
188 specifically chosen considering its broad swath and wider applicability in estimating land
189 surface temperature. MODIS LST is validated against ground observations on diverse land
190 covers and reported to provide realistic estimate of surface temperature (Wan, 2014) with an
191 uncertainty of ≤ 0.5 K. The dataset includes daytime maximum LST (at 1:30 PM local time) and
192 nighttime minimum LST (at 1:30 AM local time). Here, daytime LST dataset were obtained
193 solely from the MODIS sensor onboard the Aqua satellite to closely coincide with VIIRS fire
194 count observations at 1:30 PM local time, a period when crop residue-based fires are
195 expected to reach at peak.

196 Aerosol optical depth (AOD) from Visible Infrared Imaging Radiometer Suite (VIIRS)
197 sensor on-board SNPP satellite offers accurate estimation of columnar aerosol loading at 550
198 nm over land. Accuracy of VIIRS V1 DB AOD was evaluated extensively over South Asia by Aditi
199 et al. (2023) and reported to provide stable AOD retrieval against AERONET. Sayer et al. (2019)
200 reported an estimated error of $\pm(0.05+20\%)$ in VIIRS Version 1 DB AOD dataset. Here, Deep
201 Blue (DB) Version 1 AOD dataset (AERDB_L2_VIIRS_SNPP Level-2) was used to retrieve AOD
202 with a nominal spatial resolution of 6 km at nadir. Only quality assured AOD (QA ≥ 2) was
203 retrieved for the months of October to November over selected spatial domain.

204 Terra/Aqua MODIS land cover data was used to discriminate crop land against the rest
205 to filter out thermal anomalies exclusively over the agriculture land. To achieve this, MODIS
206 L3 V6.1 Global Land Cover type product (MCD12Q1) was retrieved from LAADS DAAC site for
207 year 2017, available at 0.5 km spatial resolution. MODIS land cover types adopts International

208 Geosphere-Biosphere Programme (IGBP) and other land type classification schemes to
209 classify land cover. Here, land cover type 12 (cropland) was earmarked to isolate the
210 agriculture land from its surrounding (Fig. S3).

211 Daily composite data on surface and root-zone soil moisture (SM, $\text{m}^3 \text{ m}^{-3}$) available at
212 9 km resolution was obtained from NASA's Soil Moisture Active Passive (SMAP) satellite
213 mission having L-band radar. The Normalized Difference Vegetation Index (NDVI) at 6 km
214 resolution was derived from the VIIRS/SNPP Deep Blue (AERDB_L2_TOA_NDVI) dataset and
215 was utilized to quantify surface vegetation greenness dynamics. Elevation data at 30 m
216 resolution was retrieved from Copernicus DEM - Global and European Digital Elevation Model
217 dataset for year 2015. Surface albedo data was acquired from MCD43 suite of NASA standard
218 product which integrates both Terra and Aqua retrievals. Here, white-sky version 6.1
219 shortwave albedo data (MCD43A3, Albedo_WSA_shortwave) at 500 m pixel resolution with
220 daily-time step (quality score: 0) was used.

221 Lower surface meteorological data including air temperature (AT), total solar radiation
222 flux (SR), precipitation (PR), relative humidity (RH) was procured from European Centre for
223 Medium-Range Weather Forecasts (ECMWF) AgERA5 dataset. The AgERA5 dataset has been
224 generated by Copernicus Climate Change Service (2020) from hourly ECMWF ERA5 dataset for
225 specific agro-ecological based applications. The meteorological data were pre-customized
226 with temporal aggregation aligned to local time zones and spatial enhancement to a 0.1°
227 resolution using grid-based variable-specific regression model. Here, air temperature at 2
228 meters above the surface, total solar radiation flux received at the surface over a 24-hour time
229 period, and relative humidity at 2 m height was selectively used over pre-identified intensive
230 crop-based fire zone. Planetary boundary layer height (PBLH) data at $0.25^\circ \times 0.25^\circ$ resolution
231 was acquired from ECMWF ERA5 for 13:00-14:00 h local time corresponding with VIIRS
232 overpass time. A description of all core datasets used in this analysis and their resolution,
233 version, and quality flags is included in Table S1 (in supplementary file).

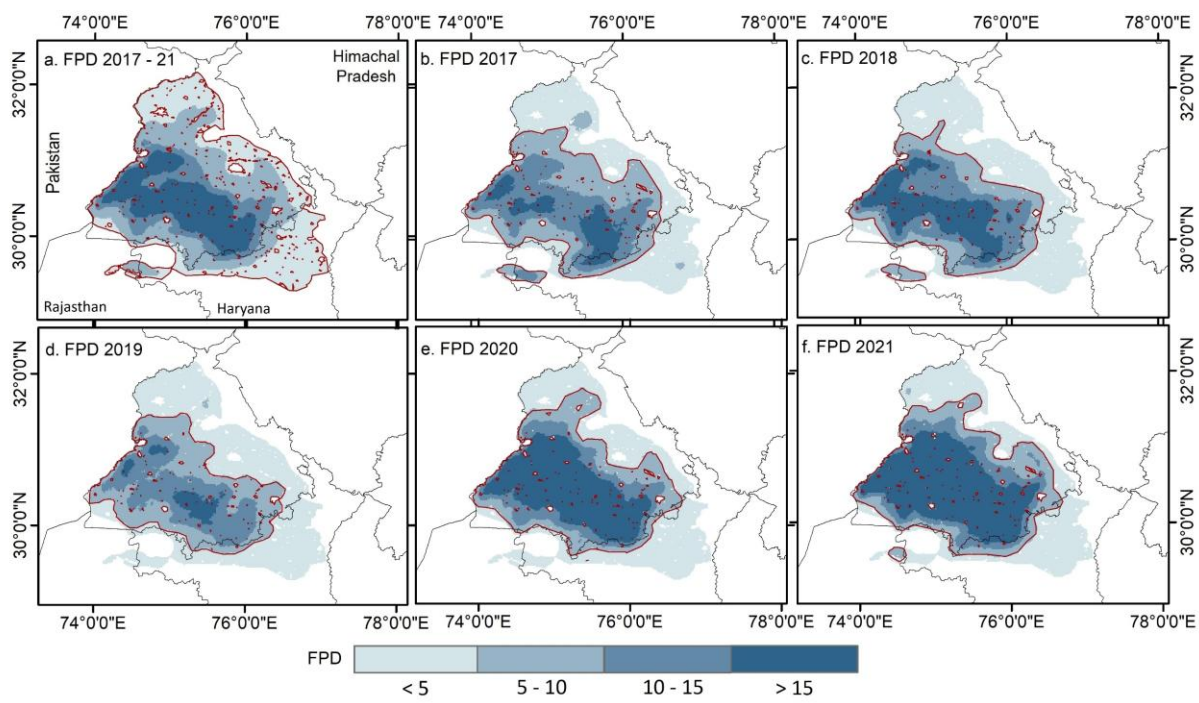
234

235 **2.3 Spatial analysis for fire-aerosols-LST association**

236 **2.3.1 Selection of intensive fire zone**

237 Post-harvest residue burning typically begins in mid-October and reaches peak
238 intensity by mid-November across northwestern India. Accordingly, all spatial analyses were

239 conducted for October and November for the years 2017–2021. The VIIRS 375 m fire product
 240 successfully retrieved active fire pixels across the Indo-Gangetic Plain, capturing substantial
 241 spatial heterogeneity. To ascertain a representative region having predominance of residue-
 242 based fire, spatial comparison of fire pixel density was made using daily retrieved VIIRS FRP
 243 dataset. FRP was selected instead of fire counts because it directly quantifies the radiative
 244 energy released from active burning and therefore provides a more meaningful metric for
 245 assessing potential impact on LST. FRP density was computed on a $1.5 \times 1.5 \text{ km}^2$ grid to
 246 characterize spatial variations in fire intensity across northwestern India. Following Giglio et
 247 al. (2006), FRP density was estimated as the ratio of total FRP within a grid cell to the grid
 248 area.



249
 250 Fig. 2. Selection of high intensity residue-based fire zone based on fire radiative power pixel
 251 density ($\text{MW } 2.25 \text{ km}^{-2} \text{ day}^{-1}$). Fig. 2a indicates the '*extended geographical region*'
 252 demarcating the entire area with varying fire intensity selected for spatial analysis. Rest
 253 of the figures classify year-specific '*intensive fire zone*' based on FRP density.
 254

255 Initially, geospatial variations in fire intensity and the associated changes in LST and
 256 AOD were evaluated. Spatial intercomparison between FRP, LST, and AOD was performed
 257 over the region delineated in Fig. 2a. This area was selected to encompass an extended
 258 geographical domain without imposing thresholds on low or high FRP density across
 259 northwestern India. The region is hereafter referred to as the "extended geographical

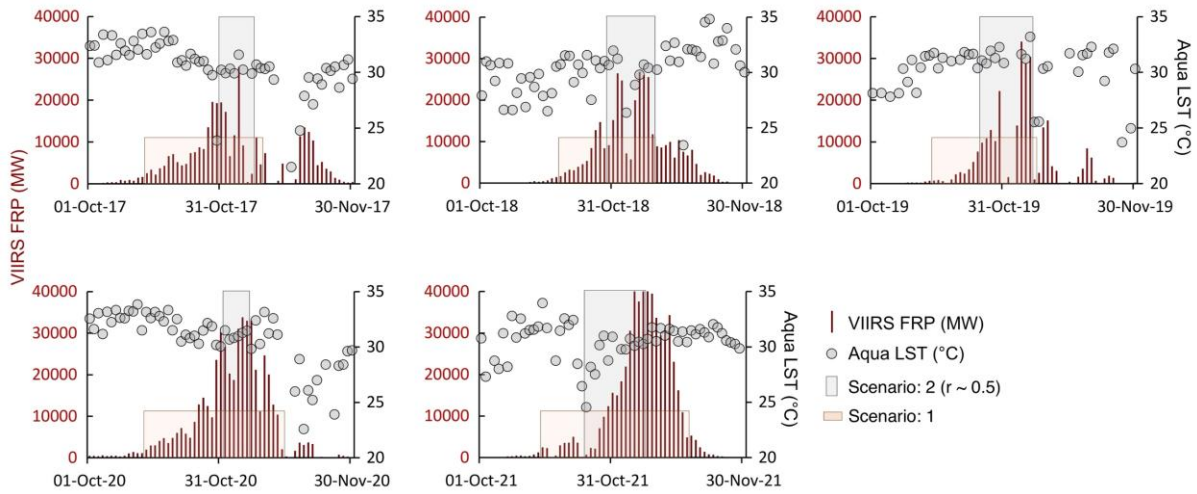
260 region,” as it integrates fire activity across all years and was used exclusively to establish the
261 spatial association between the predictor (FRP) and dependent variables (LST and AOD).

262 In contrast, to assess the day-to-day influence of fire intensity and aerosol loading on
263 LST, a comparatively high-intensity fire zone was delineated relative to low-intensity areas.
264 To achieve this, the entire crop-residue burning region of northwestern India was mapped
265 using a constraint from low FRP density ($<5 \text{ MW grid}^{-1}$) to high FRP density ($>15 \text{ MW grid}^{-1}$).
266 Spatial variations in FRP density were evaluated for each year, and regions with FRP density
267 $>5 \text{ MW grid}^{-1}$ were identified as the “intensive fire zone” (Fig. 2b–f). This threshold ensured a
268 better representation of the effect of medium to large crop-based fire on regional LST as
269 small-intensity fire deem to extinguish faster while being inconducive to considerably
270 influence surface temperature (Zhao et al., 2024).

271 All subsequent spatial datasets used for evaluating FRP–AOD–LST relationships were
272 retrieved exclusively within the year-specific ‘intensive fire zone’ having FRP density $>5 \text{ MW}$
273 grid^{-1} . Notably, the spatial extent of the high-FRP region remained largely consistent across all
274 years (Fig. 2b–f), with areal estimates summarized in Table S2. It is noteworthy, the region was
275 pre-filtered based on the Terra/Aqua MODIS land cover data to deselect any FRP pixel that
276 emerged from a non-agricultural/crop land.

277 **2.3.2 Selection of temporal window**

278 After isolating the region with higher fire pixel density, the next step was to identify
279 the temporal window in which potential associations between fire intensity and other
280 explanatory variables could be examined. The temporal selection was based on two scenarios,
281 as illustrated in Fig. 3. Scenario 1 was designed to quantify the influence of FRP, aerosols, and
282 other parameters on LST during the period when fire activity begins to intensify and remains
283 persistent over the intensive fire zone. Scenario 1 defines the initiation day as the first instance
284 in October when aggregate FRP consistently exceeds 1500 MW and shows at least a 50%
285 increase compared to the previous day. The scenario concludes in November when aggregate
286 FRP decreases by at least 50% relative to the previous day. The selected dates for Scenario 1
287 are listed in Table S3, with two exceptions. First, in year 2018 when a $>50\%$ criteria was not
288 met despite having an aggregate FRP $>1500 \text{ MW}$ and second, in year 2017 when a prior
289 decrease ($>50\%$) in FRP was avoided because of subsequent rise in fire intensity.
290



291

292 Fig. 3. FRP and LST time series over intensive fire zone showing the extent of scenarios used
293 for geospatial modelling.

294 To define Scenario 2, a statistical association was examined between day-specific
295 aggregate FRP and the spatially averaged LST. Pixel-based LST values were averaged over the
296 intensive fire zone and compared against the area-weighted sum of FRP on a day-to-day basis.
297 A temporal window (“Scenario 2” in Fig. 3) was selected using two criteria: (i) the end of the
298 window had to coincide with a period of persistently high FRP, and (ii) the window had to
299 exhibit a strong positive correlation ($r \geq 0.5$) between FRP and regional LST. Such restricted
300 criteria were put to ensure that we only select year-specific window(s) when FRP (so the fire
301 count) increases with time and exhibit a strong association with regional LST. Descriptive
302 statistics of both scenarios are included in Table S4. It is noteworthy that selecting multiple
303 windows within a year having coinciding days was avoided while ensuring windows should not
304 contain more than 5% of missing days, irrespective of parameters.

305 **2.4 Spatial correlation between fire, aerosols and LST**

306 To examine the spatial association among FRP, LST, and AOD over the residue-based
307 fire zone, grid-based spatial correlation coefficients were computed, and their statistical
308 significance ($p < 0.05$) was tested across the study domain. Daily FRP (375 m) and LST (1 km)
309 datasets were initially resampled to a $6 \times 6 \text{ km}^2$ resolution to match the VIIRS AOD dataset
310 before subject to spatial correlation analyses among the predictor and dependent variables.
311 This approach facilitated the identification of regions exhibiting strong co-variability in thermal
312 conditions corresponding to variations in fire intensity and columnar aerosol loading.

313 **2.5 Hurst Exponent**

314 The Hurst exponent is a statistical measure used to characterize the properties of a
315 time series without imposing assumptions about its underlying distribution. Originally
316 introduced by Hurst (1951) in hydrological studies and later refined by Markonis and
317 Koutsoyiannis (2016), it has since been widely applied across diverse scientific disciplines to
318 analyse long-term trends and variability. In this study, the Hurst exponent was computed for
319 FRP, AOD, and LST time series to identify long-term statistical persistence in the datasets. To
320 estimate the Hurst exponent at the spatial scale, $6 \times 6 \text{ km}^2$ resampled datasets of FRP, AOD,
321 and LST were used. Adjustment of seasonal cycle was not accounted, as the datasets were
322 retrieved and processed exclusively for a single season across the selected years. The main
323 calculation procedures were as follows (Granero et al., 2008):

324 A time series $x(t)$ is given,

325
$$(x)_t = 1/\tau \sum_{t=1}^{\tau} x(t) \quad t = 1, 2, 3 \dots \quad (1)$$

326 The cumulative deviation is determined using Eq. 2:

327
$$X(t, \tau) = \sum_{u=1}^{\tau} (x(u) - (x)_t), \text{ with a condition of } 1 \leq t \leq \tau. \quad (2)$$

328 Extreme deviation sequence, is defined as:

329
$$R(\tau) = \max_{1 \leq t \leq \tau} X(t, \tau) - \min_{1 \leq t \leq \tau} X(t, \tau) \text{ where } \tau = 1, 2, 3 \dots \quad (3)$$

330 The standard deviation sequence is calculated by Eq. (4):

331
$$S(\tau) = [1/\tau \sum_{t=1}^{\tau} (x(t) - (X)_\tau)^2]^{1/2} \text{ where } \tau = 1, 2, 3 \dots \quad (4)$$

332 By considering both extreme deviation sequence and standard deviation sequence,

333
$$R/S = R(\tau)/S(\tau) \text{ when assuming } (R/S) \propto (\tau/2)^H \quad (5)$$

334 The Hurst exponent ranges between 0 and 1. A value of 0.5 indicates that the time
335 series behaves as a purely stochastic process without persistence, implying that future
336 variations are independent of past behaviour. Values greater than 0.5 denote statistical
337 persistence, reflecting a tendency for future changes to follow the same trend as in the past,
338 with higher values corresponding to stronger persistence. Conversely, values below 0.5
339 indicate anti-persistence, suggesting a tendency for the time series to reverse its trend over
340 time; lower values represent stronger anti-persistence (Peng et al., 2011).

341 **2.6 Space-for-time approach**

342 A space-for-time approach was employed to assess and compare the changes in LST
343 and AOD with respect to FRP within the extended geographical region experiencing recurrent
344 medium- to high-intensity fire. To ensure that changes in LST and AOD were attributable solely
345 to fire activity, grids with similar characteristics in terms of topography, climate, and physical
346 environment were compared (Liu et al., 2019). To achieve this, daily datasets including
347 meteorological covariates (PBLH, AT, SR, RH and PR), physical environment (elevation),
348 vegetation and soil characteristics (NDVI, soil moisture), climatological mean LST and AOD,
349 and surface property (albedo) were extracted over both fire and no-fire grids at a spatial
350 resolution of $10 \times 10 \text{ km}^2$. The daily data were retrieved for each grid under Scenario 2, when
351 FRP reached its peak and exhibited a positive association with regional LST.

352 After filtering out the grid cells with missing LST or AOD values, remaining grids were
353 classified into two groups: those with zero FRP (no-fire) against the grids having $\text{FRP} > 0$,
354 indicating presence of fire. Fire and no-fire grids with comparable spatial characteristics were
355 grouped into a single stratum, and a stratified matching technique was applied to generate
356 multiple strata based on combinations of the selected confounders. Grids were retained only
357 when differences in their physical environment, vegetation and soil characteristics, climate
358 and land cover between fire and no-fire conditions were smaller than the defined thresholds
359 ($\Delta\text{elevation} < 50 \text{ m}$; $\Delta\text{NDVI} < 0.05$; $\Delta\text{soil moisture} < 0.05$; $\Delta\text{albedo} < 0.05$; $\Delta\text{LST} < 10.0$; $\Delta\text{AOD} < 0.80$). Comparisons were then made within strata containing grids of similar attributes to
361 ensure that the observed variations in LST and AOD could be attributed solely to fire activity.
362 The difference in LST (ΔLST) among the fire grids (LST_{fire}) and grids exhibiting no-fire ($\text{LST}_{\text{no-fire}}$)
363 having similar attributes were compared to constitute effect of residue-based fire on LST. A
364 positive (negative) ΔLST ($\text{LST}_{\text{fire}} - \text{LST}_{\text{no-fire}}$) indicates fire-induced warming (cooling) and was
365 used to quantify changes in LST associated with residue burning for the selected years. A
366 similar approach was also adopted to evaluate ΔAOD variations using grid-based retrievals.

367 It is noteworthy that the grids were not classified based on meteorological covariates,
368 as only insignificant variations were noted among the grids. The entire northwestern cropland
369 experiences a relatively uniform background climate during October–November, including
370 comparable boundary layer heights, with PBLH standard deviations ranging from $\pm 10 \text{ m}$ to
371 $\pm 33 \text{ m}$ within a single fire season. The climatological mean LST and AOD were computed only

372 for the pre-fire season (September, 2017-2021), during which none of the grids experienced
373 residue-burning activity. Furthermore, grids were not differentiated by slope or aspect, given
374 the minimal topographic variation across the Gangetic Plain.

375 **2.7 Multicollinearity assessment**

376 Multicollinearity, where independent variables are highly correlated, can distort
377 regression estimates and obscure the true contribution of individual predictors (Graham,
378 2003). To assess this, the Variance Inflation Factor (VIF) for all covariates was calculated using
379 the *statsmodels* library. A VIF of 1 indicates no correlation, values between 1 and 5 suggest
380 moderate correlation, and values greater than 5 are generally interpreted as evidence of
381 substantial multicollinearity (Daoud, 2017). All biophysical, land-surface, and meteorological
382 variables met acceptable VIF thresholds, except solar radiation, which was therefore excluded
383 from Random Forest and GWR analysis. Additionally, soil moisture data was removed from
384 further analysis due to a high percentage of missing observations (~30%).

385 **2.8 Random Forest regression**

386 Random Forest regression was used to model the relationship between the
387 dependent variable (LST) and predictor variables (AOD, PBLH, AT, RH, SR, PR, NDVI, elevation,
388 albedo, and FRP) within the intensive fire zone. Daily retrievals, averaged over the year-
389 specific intensive fire area, were incorporated into the ensemble framework to capture
390 potential non-linear associations among variables. The selected approach ensures robustness
391 to multicollinearity, minimizes overfitting, and effectively captures complex predictor
392 interactions.

393 Random Forest is a non-linear ensemble machine learning algorithm that constructs
394 multiple decision trees from bootstrapped samples of the training data, with a random subset
395 of predictors evaluated at each split. Final predictions are obtained by averaging all trees,
396 improving generalization and reducing overfitting (Breiman, 2001; Puissant et al., 2014). The
397 algorithm was selected due to its strong predictive capability, scalability to large
398 environmental datasets, resilience to correlated inputs, and demonstrated success in
399 previous LST-related studies (Logan et al., 2020; Wang et al., 2022; Zhang et al., 2025). These
400 attributes collectively support Random Forest as an appropriate and interpretable choice for
401 assessing the complex interactions between fire intensity, aerosol loading, and LST dynamics.

402 Key Random Forest hyperparameters (`n_estimators`, `max_depth`, `min_samples_split`,
403 `min_samples_leaf`, and `max_features`) were optimized using Bayesian optimization
404 implemented via `BayesSearchCV` in *scikit-optimize* (Snoek et al., 2012; Shahriari et al., 2015;
405 Frazier, 2018). This adaptive, probabilistic search strategy efficiently identifies near-optimal
406 hyperparameter combinations while minimizing computational cost. To ensure robust model
407 evaluation and mitigate temporal dependence, we employed temporal block cross-validation
408 using a 3-fold `GroupKFold` in the *scikit-learn* library, where all observations from a given year
409 were assigned to the same fold. This approach prevented temporal overlap between training
410 and validation datasets and reduced information leakage across years. This approach also
411 minimized temporal autocorrelation and prevented data leakage across time periods. Model
412 performance was quantified using cross-validated coefficient of determination (R^2), Root
413 Mean Squared Error (RMSE), and Mean Absolute Error (MAE), providing a comprehensive
414 assessment of model accuracy and prediction error.

415 **2.9 Assessment of relative feature importance**

416 Variable importance was derived from the trained RF model using the mean decrease
417 in impurity method, which quantifies each predictor's relative contribution to reducing
418 variance in model predictions. This approach provides insight into the dominant factors
419 governing the spatial and temporal variability of LST. Feature importance values were
420 extracted and ranked to identify the most influential predictors under different fire intensity
421 scenarios. To enable direct comparison among predictors, the relative contribution of each
422 feature was expressed as its importance score normalized by the sum of all feature
423 importances. As Scikit-learn's `RandomForestRegressor.feature_importances_` inherently
424 returns normalized values summing to one, the reported scores directly represent each
425 predictor's proportional influence within the model.

426 **2.10 Spatial heterogeneity assessment using GWR**

427 Spatial heterogeneity in the influence of FRP, AOD, and other spatial predictors on LST
428 within the intensive fire zone was assessed using Geographically weighted regression (GWR)
429 at 1x1 km² grid. GWR is a spatially explicit regression technique designed to quantify how
430 relationships between predictors and a dependent variable vary across geographic space by
431 estimating spatially varying coefficients (Brunsdon et al., 1996). The method applies a
432 distance-based weighting scheme, whereby observations closer to a given location receive

433 higher weights, allowing local parameter estimation that reflects neighbourhood-specific
434 dynamics (Yang et al., 2020). Unlike global regression models that assume spatial stationarity,
435 GWR produces location-specific coefficient estimates, offering a more nuanced
436 understanding of spatially varying associations between LST and its predictors (Fotheringham
437 et al., 2009). The GWR model is formally expressed as:

438
$$y_i = \beta_0(u_i, v_i) + \sum_{k=1}^m (\beta_k(u_i, v_i) x_{ik}) + \varepsilon_i \quad (6)$$

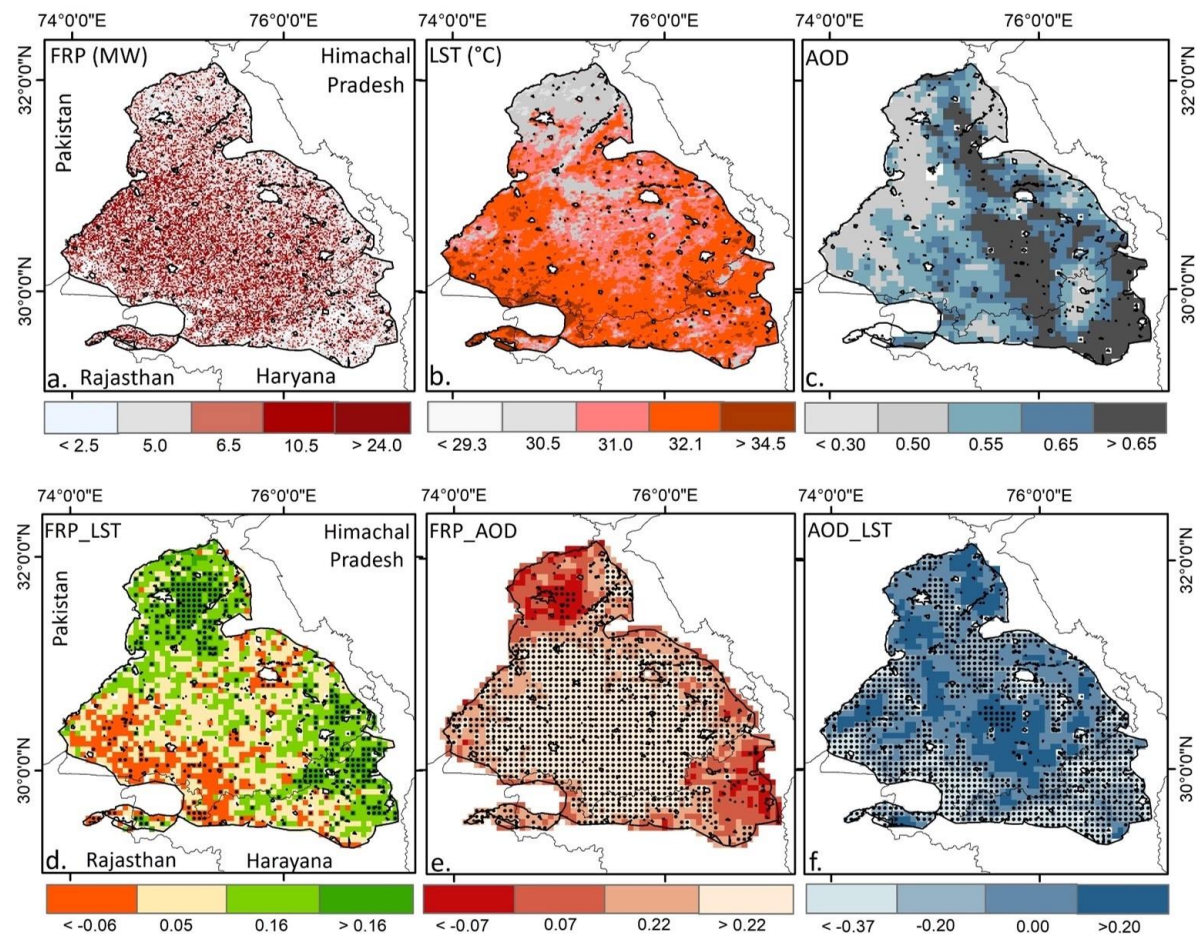
439 where (u_i, v_i) are the coordinates of observation i , $\beta_k(u_i, v_i)$ are spatially varying coefficients,
440 x_{ik} are predictor variables, and ε_i denotes random error. In GWR, local parameters are
441 estimated using weighted least squares, where each observation is assigned a weight based
442 on its spatial proximity to the location being evaluated. These weights are determined by a
443 spatial kernel function and a bandwidth parameter that defines the extent of spatial
444 influence. Selecting an optimal bandwidth is therefore essential to balance the trade-off
445 between model bias and variance. In this study, the optimal bandwidth was identified through
446 an iterative optimization procedure that minimizes the corrected Akaike Information
447 Criterion (AICc) (Fotheringham et al., 2009). This approach ensures robust estimation of local
448 relationships while effectively accounting for spatial non-stationarity in the dataset. Such a
449 framework is particularly valuable in fire-affected landscapes, where the impacts of fire
450 intensity, aerosol loading, and surface characteristics on LST are inherently heterogeneous
451 and vary substantially across space.

452 **3. Results and discussions**

453 **3.1 Spatial association between fire, aerosols and LST**

454 Spatial variations in FRP, LST and AOD averaged for October to November between
455 2017 and 2021 over extended geographical region is shown in Figure 4(a-c). While residue-
456 based FRP did not exhibit a distinct spatial pattern, temporal variations were prominent, with
457 monthly mean FRP in November ($310,188 \text{ MW month}^{-1}$) showing nearly a 100% increase
458 compared to October ($152,616 \text{ MW month}^{-1}$; Table S5). In contrast, the spatial pattern of LST
459 exhibited considerable heterogeneity, with relatively higher temperature observed in the
460 southern parts of the region that gradually declined northward. This north–south gradient
461 may be partially attributed to the proximity of the Himalayan foothills, where the cooler
462 mountainous environment likely offsets fire-induced surface warming. A gradual decline in

463 spatially averaged monthly mean LST was also accounted in November (29.0 ± 2.4 °C)
 464 compared to October (31.0 ± 1.6 °C). A spatially distinct pattern in columnar aerosol loading
 465 was evident across the extended geographical region, with elevated AOD (> 0.65) retrieved
 466 over the central areas that gradually decreased towards its periphery (< 0.30). Such spatial
 467 variability in aerosol loading is likely driven by differences in the intensity of residue-based
 468 fires and the associated emissions of aerosols and trace gas precursors. Moreover, the
 469 pronounced increase in monthly mean AOD (October: 0.59 ± 0.08 ; November: 0.82 ± 0.12)
 470 likely reflects the intensification of fire during early November, compounded by concurrent
 471 meteorological influences, most notably the seasonal decline in boundary layer height
 472 (Banerjee et al., 2022).



473
 474 Fig. 4. Spatial variations of FRP, LST and AOD over extended geographical region, 5-year mean
 475 FRP (a), LST (b) and AOD (c), and spatial correlation between FRP_LST (d), FRP_AOD (e)
 476 and AOD_LST (f). To compute spatial correlation, daily retrievals of FRP, AOD and LST
 477 were converted to a common 6×6 km 2 grid. Spatial correlation was computed for the
 478 entire duration and significant correlation ($P < 0.05$) is shown with black dot.

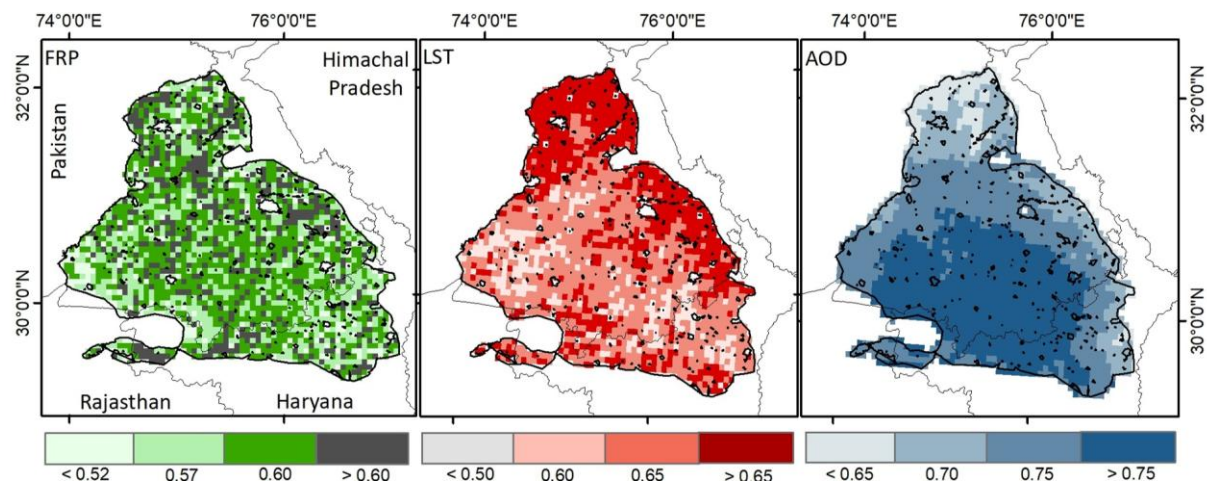
479
480 Spatial associations among VIIRS-derived FRP, MODIS LST, and VIIRS-based AOD daily
481 retrievals were assessed over the extended geographical region (Fig. 4d–f). Spatial correlation
482 between pixel-based FRP against LST reveals positive but spatially heterogenous association
483 across most parts of the study area, except in the southern region. A statistically significant
484 relationship ($P < 0.05$) between FRP and LST underscores the potential influence of crop
485 residue burning on surface temperature. Similarly, a significant association between FRP and
486 AOD was observed across the central region, where fire intensity was notably higher than in
487 surrounding areas. This spatial covariation between fire intensity and columnar aerosol
488 loading further reinforces the influence of biomass-burning-induced emissions of aerosols
489 and their precursors on atmospheric aerosol abundance. Biomass-burning aerosols,
490 predominantly composed of carbonaceous soot particles, are known to modulate the thermal
491 budget of the lower atmosphere (Freychet et al., 2019; Xu et al., 2021). The spatial association
492 between AOD and LST further supports the existence of a fire–aerosol–surface temperature
493 nexus over northwestern India. A comparatively weak yet statistically significant positive
494 correlation between AOD and LST likely reflects lower-atmospheric warming induced by
495 smoke aerosols, consistent with the similar warming effect over western United States during
496 2017 California wildfire (Gomez et al., 2024).

497 **3.2 Evaluation of Hurst exponent**

498 The Hurst exponent was evaluated to assess the long-term persistence of fire
499 intensity, surface temperature, and aerosol loading time series over the extended
500 geographical region. In principle, the Hurst exponent is used to quantitatively distinguish a
501 purely stochastic time series ($H = 0.50$) from a persistent ($H > 0.50$) or anti-persistent ($H <$
502 0.50) time series of pixel-based FRP, LST, and AOD, following the methodology described in
503 Markonis and Koutsoyiannis (2016) and Chen et al. (2022).

504 As shown in Figure 5, nearly the entire extended geographical region of northwestern
505 India exhibits Hurst exponent values greater than 0.50 for FRP, with relatively higher values
506 (0.60–0.70) concentrated toward its central zone. Although variations in Hurst exponent for
507 FRP was spatially inconsistent, primarily due to temporal and spatial fluctuations in fire
508 intensity, the FRP time series over most of the region indicates statistical persistence.
509 Similarly, elevated Hurst exponent values for LST (>0.50) across the region also exhibits

510 persistence at long run. Notably, the northern portion of the study region shows slightly
 511 higher Hurst exponent values compared to the southern part. For regional aerosol loading,
 512 except few isolated patches, comparatively high Hurst exponent values (>0.75) were
 513 observed over the central region. Notably, this area also coincides with zones characterized
 514 by high AOD (>0.65) and a statistically significant FRP–AOD association. Overall, the Hurst
 515 exponent analysis indicates that the observed FRP, LST, and AOD time series across most of
 516 the residue-burning region exhibit statistical persistence.

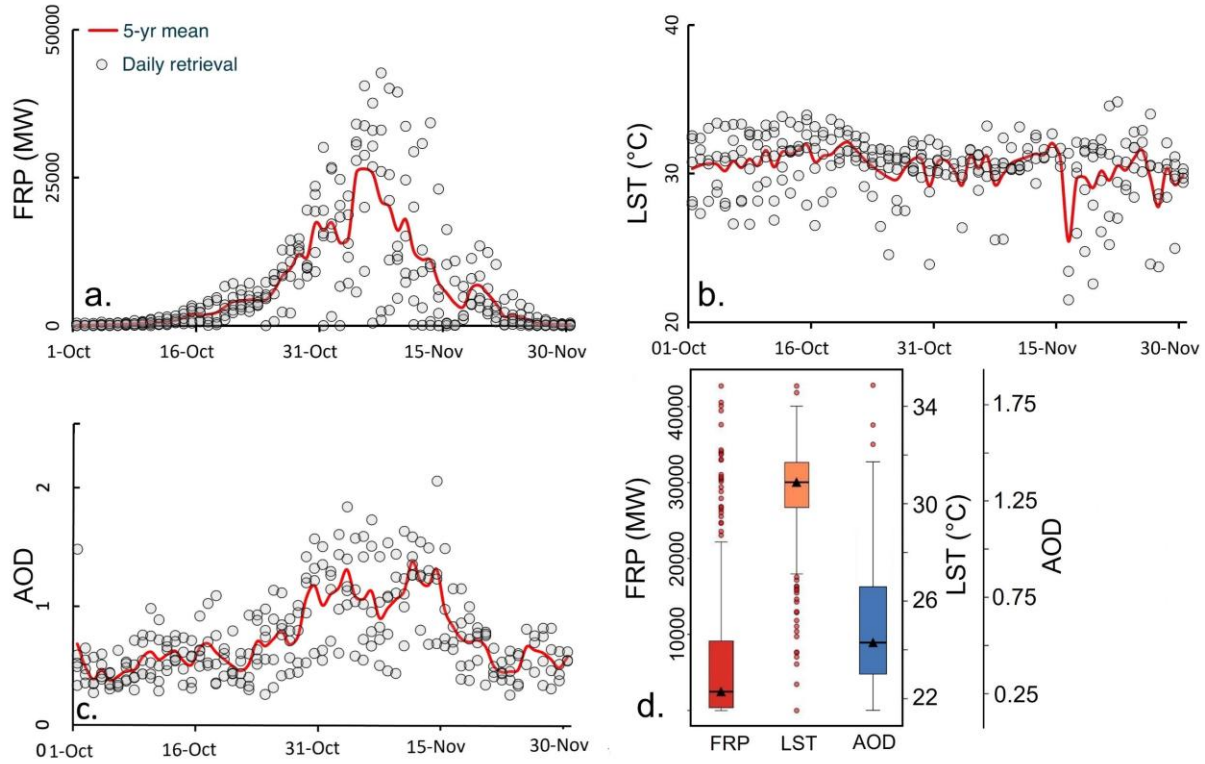


519 Fig. 5. Estimating FRP (MW), LST ($^{\circ}\text{C}$) and AOD time-series persistence in extended
 520 geographical region.

521 However, interpretation of the Hurst exponent results should be approached with
 522 caution. The five-year dataset used here may not be sufficient to derive statistically robust
 523 estimates. For the same reason, trend analysis was not undertaken, as the limited dataset
 524 constrains the reliability of such estimates and falls beyond the scope of the present study.
 525 Nonetheless, several studies have documented long-term trends in fire dynamics and aerosol
 526 loading over northwestern India (e.g., Vadrevu and Lasko, 2018; Jethva et al., 2019; Singh et
 527 al., 2020).

528 3.3 Surface temperature and aerosols response to fire intensity

529 Fire intensity in terms of pixel-based FRP, aerosol loading and surface temperature
 530 were retrieved to compute corresponding daily and spatial means based on five years of
 531 satellite retrievals. It is noteworthy that to account immediate response of fire intensity and
 532 aerosol loading on surface temperature, all variables were retrieved exclusively over year-
 533 specific intensive fire zones, having cumulative FRP $\geq 5 \text{ MW grid}^{-1}$, as illustrated in Fig. 2(b-f).



534

535 Fig. 6. Time series of five-year mean fire radiative power (FRP, a), land surface temperature
 536 (LST, b) and aerosol optical depth (AOD, c) against daily retrievals, (d) covariation of FRP,
 537 AOD and LST over intensive fire zone. Gray dots show daily retrievals from October to
 538 November (2017–2021), with the red line depicting the corresponding 5-year mean.

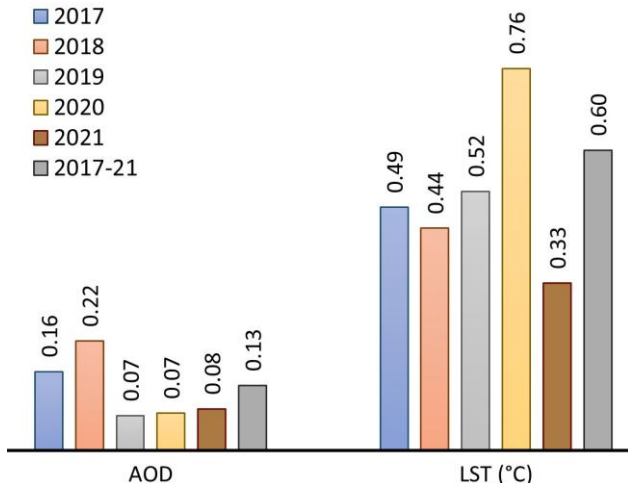
539 A distinct temporal pattern is evident in the FRP time series (Fig. 6a), which corresponds
 540 closely with daily variations in fire counts (Fig. S4). Over northwestern India, FRP starts to
 541 build-up typically in mid-October, peaks consistently during the first week of November, and
 542 declines thereafter by mid-November. In contrast, the temporal pattern of the five-year mean
 543 LST time series appears less pronounced, as daily retrievals exhibit substantial variability.
 544 Regional LST demonstrates both interannual and intra-annual fluctuations, as illustrated in
 545 Fig. S5. Notably, the FRP time series aligns well with the mean columnar aerosol loading,
 546 underscoring the potential influence of aerosol and precursor emissions from widespread
 547 biomass burning. The characteristic rise in AOD during the first two weeks of November likely
 548 represents a direct response to intensified fire activity, as columnar AOD values consistently
 549 exceed 1.00 over the intensive fire zone. Interestingly, between October 25 and November
 550 20 each year, approximately 90% of daily AOD observations surpass the five-year mean (0.74 ± 0.28), coinciding with an 800% increase in average FRP ($13,085 \pm 6,825$ MW) compared to

552 the remainder of the season ($1,148 \pm 1,478$ MW). During this interval, the five-year mean
553 columnar AOD exhibits a strong association with the aggregate FRP ($r = 0.46$) and mean LST
554 ($r = 0.41$), whereas these associations weaken considerably outside this period (AOD–FRP: $r =$
555 0.18 ; AOD–LST: $r = -0.02$).

556 The temporal associations among FRP, AOD, and LST clearly demonstrate the
557 immediate response of fire-induced variations in aerosol loading and surface temperature
558 over northwestern India. Accordingly, in the subsequent section, these relationships were
559 modelled using a geospatial tree-based regression framework that integrates concurrent
560 temporal features (e.g., day-specific retrievals) and spatial predictors (e.g., regional
561 meteorology, aerosol loading, and fire intensity) to quantify and characterize the FRP–AOD–
562 LST nexus within the intensive fire zone.

563 **3.4 Fire induced change in LST and AOD**

564 The effect of crop residue burning on land surface temperature and aerosol loading
565 was assessed using a space-for-time approach by overlaying grid-based VIIRS LST, FRP, and
566 AOD datasets over the northwestern region experiencing recurrent fire. To remove potential
567 confounding effect, fire and no-fire grids were retained for comparison only when they
568 matched in terms of topography, meteorology, physical environment, vegetation and soil
569 characteristics, climatological mean LST and AOD, and surface property. Comparisons were
570 performed within defined strata containing grids with identical characteristics to ensure that
571 the quantified changes in LST and AOD could be attributed solely to fire. A total of 7489 paired
572 no-fire and fire grids were used between 2017 and 2021 to quantify the relative change in LST
573 and AOD. It is noteworthy that all grids, whether exhibiting fire or not, were selected from
574 within the extended geographical region to capture localized variations in temperature and
575 aerosol loading.



576
577 Fig. 7. Crop residue-based fire induced changes in land surface temperature and aerosol
578 loading.

579 As illustrated in Fig. 7, a consistent yet temporally dynamic increase in both LST and
580 AOD was observed over regions affected by residue-based burning compared with no-fire
581 zone. However, the magnitude of LST and AOD change across the fire zone was spatially
582 heterogeneous. On average, residue-based burning induced an increase of 0.60 °C in LST
583 during 2017–2021, with interannual variability ranging from 0.33 °C to 0.76 °C. This indicates
584 that residue burning exerts a persistent warming influence on land surface temperature, likely
585 driven by reduced evapotranspiration, enhanced shortwave absorption, increased sensible
586 heat flux, and fire-induced changes in surface albedo. However, a strong spatial heterogeneity
587 in LST and AOD modulation further indicates the potential influence of key confounding
588 factors and intensity of fire in regulating the change. The results of this study align with Liu et
589 al. (2019), who attributed a 0.15 °C rise in surface temperature over burned areas globally to
590 satellite-observed forest fires, as well as Liu et al. (2018), who documented a net warming
591 effect over the Siberian boreal forest. Additional evidence from Alkama and Cescatti (2016)
592 and Zhao et al. (2024) also indicates a positive linkage between forest fire occurrence, fire
593 intensity, and surface temperature. In contrast, the biophysical effects of agricultural residue
594 burning on land surface temperature remain poorly constrained. Zhang et al. (2020) reported
595 LST increases of 1–3 °C over three provinces in China associated with crop residue burning.
596 However, the feedback effects of meteorological covariates and systematic land-cover
597 differences on fire occurrence were not accounted for, leading to causal attribution of fire to
598 LST remains tentative.

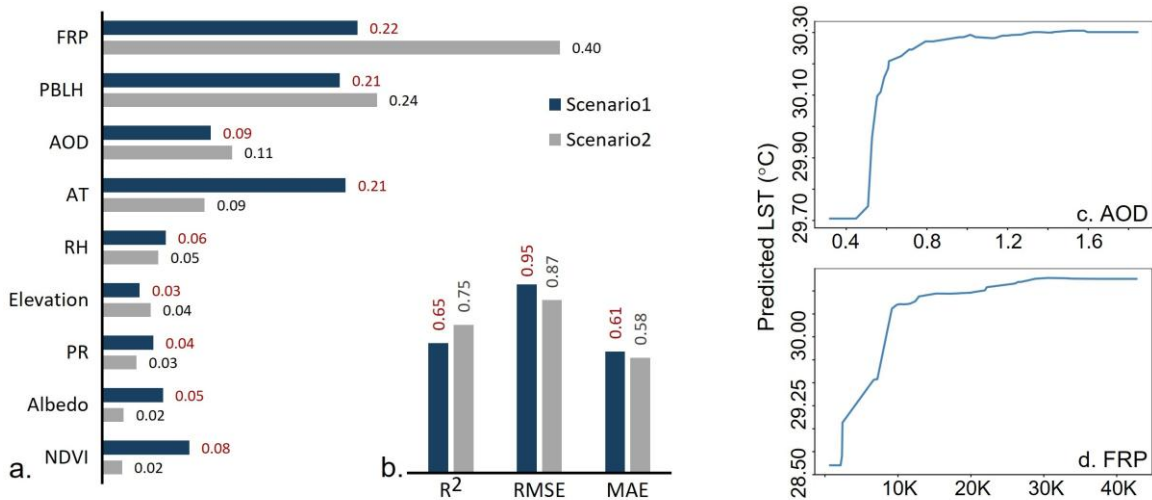
599 A consistent annual increase in aerosol loading was also observed over the fire-
600 affected grids over northwestern India. A clear upward trend in AOD was noted across the
601 fire zones, with a mean increase of $0.13 \text{ AOD year}^{-1}$ and a range of $0.07\text{--}0.22 \text{ AOD year}^{-1}$. The
602 change in columnar aerosol loading, however, was spatially heterogeneous. Overall, the
603 increase in AOD from fire-associated emissions of aerosols and their gaseous precursors
604 reinforces the source-specific contribution of crop residue burning, a phenomenon well
605 documented in previous studies (Vinjamuri et al., 2020; Mhawish et al., 2022).

606 To quantify uncertainty in the estimated differences between fire-affected and non-
607 fire-affected grid cells, we further computed 95% confidence intervals for ΔLST and ΔAOD
608 using nonparametric bootstrapping. For each variable, 10,000 bootstrap samples were
609 generated by resampling grid cells with replacement, and the mean difference was
610 recalculated for each bootstrap replicate. The 2.5th and 97.5th percentiles of the resulting
611 sampling distribution were taken as the bounds of the 95% confidence interval (CI).
612 Nonparametric bootstrapping results into significant increase in both ΔLST (0.57°C ; 95% CI:
613 $0.33\text{--}0.81^\circ\text{C}$) and ΔAOD (0.13 ; 95% CI: $0.08\text{--}0.17$) in fire-affected regions. Because both CIs
614 do not overlap zero, these differences are statistically robust and unlikely to be due to
615 sampling variability.

616 **3.5 Spatial regression of fire intensity and aerosols on LST**

617 A machine learning algorithm was employed to establish the statistical association
618 between the dependent variable LST and multiple predictors including fire radiative power,
619 aerosol loading, regional meteorology (Fig. S6), surface properties, and vegetation
620 characteristics. All biophysical parameters, except SR and soil moisture, retrieved under two
621 pre-defined scenarios, (one) days with moderate-to-high fire intensity and (two) days with
622 sustained high fire intensity exhibiting a positive association with regional mean LST, were
623 used to model the FRP–AOD–LST relation. Relative feature importance (RFI) of selected
624 predictors was first evaluated for the fire season, and the marginal effects of FRP and aerosols
625 on LST were subsequently quantified. Figure 8(a) presents the normalized RFI values for all
626 predictors under both scenarios, and the Random Forest hyperparameter tuning procedure
627 is summarized in Table S6. RFI quantifies the sensitivity of regional LST to each predictor and
628 reflects their partial contribution to surface temperature variability. Fire radiative power
629 emerged as the dominant predictor under both scenarios, indicating the strong influence of

630 fire-related energy release on regional radiative balance, likely through reduced
 631 evapotranspiration and fire-induced changes in surface albedo (Liu et al., 2018, 2019).
 632 Notably, the RFI was substantially higher during period of sustained high-intensity burning
 633 (Scenario 2; RFI = 0.40) compared with days characterized by moderate-to-high fire activity
 634 (Scenario 1; RFI = 0.22), highlighting the stronger thermal response associated with intensive
 635 burning condition.



636
 637 Fig. 8. Normalized relative feature importance of predictor variables on LST (a), cross-
 638 validated evaluation of random forest performance (b), and partial dependence plots
 639 of LST on AOD (c) and FRP (d). Here, K indicates $\times 1000$. The PDP plots are based on
 640 scenario 2. Both RMSE and MAE have unit $^{\circ}\text{C}$.

641 Next to FRP, PBLH exerted a significant influence on LST (RFI: 0.21–0.24), followed by
 642 atmospheric temperature (RFI: 0.09–0.21). The strong effect of PBLH on LST can be explained
 643 by restricted turbulent mixing during shallow boundary-layer conditions in post-monsoon
 644 season. A relatively low PBLH (mean \pm SD: 71 ± 29 m) over northwestern India reduces vertical
 645 mixing and traps fire-induced heat and aerosols close to the surface (Vinjamuri et al., 2020).
 646 This enhances shortwave absorption, suppresses evaporative cooling, and limits turbulent
 647 heat dissipation, resulting in a stronger and more persistent increase in LST. Another notable
 648 finding was the modification of LST due to enhanced columnar aerosol loading during fire
 649 season. The RFI of AOD varies from 0.09 to 0.11, indicating its influence on regional radiative
 650 budget. Residue burning releases aerosols and their gaseous precursors, which can exert
 651 significant radiative impacts and drive rapid adjustments in both surface and atmospheric
 652 temperature (Freychet et al., 2019; Xu et al., 2021). Fire-generated aerosols influence the

653 energy balance through scattering and absorption of radiation, alterations in cloud
654 microphysics, and changes in surface albedo via deposition of carbonaceous particles.
655 However, the magnitude and direction of these radiative effects remain uncertain at the
656 global scale (Tian et al., 2022). The partial influence of all other parameters, including
657 meteorological variables, land characteristics and elevation was less significant (RFI < 0.30).

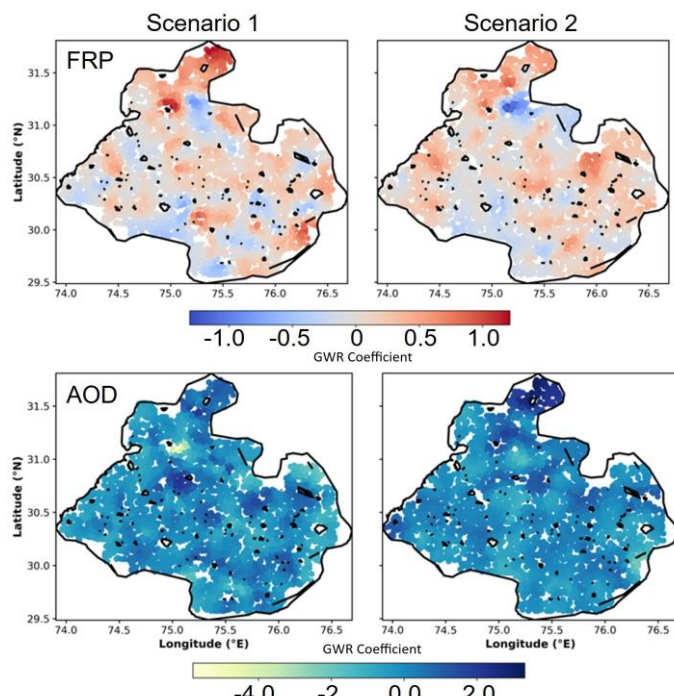
658 The predictive skill of the random forest model was assessed using temporal block
659 cross-validation to minimize temporal autocorrelation and prevent data leakage. Under both
660 scenarios model performance was found satisfactory with R^2 varying from 0.65-0.75, marked
661 with relatively low RMSE (0.87-0.95 °C) and MAE (0.58-0.61 °C). A satisfactory model
662 performance also ensures that residue burning provide a clear LST response and the RF model
663 was able to resolve non-linear land-atmosphere interactions, irrespective of the selected
664 scenarios. Relatively better performance was however, achieved in scenario 2 during the fire
665 days having better spatial association between FRP and LST. Collectively, this confirms that
666 moderate-to-high intensity residue burning leaves a measurable and predictable thermal
667 signature on the land surface over northwestern India.

668 The partial dependence plots (PDPs) in Fig. 8(c-d) illustrate the marginal effects of FRP
669 and AOD on LST. These plots show the expected change in LST associated with variation in
670 each predictor while holding all other predictors constant. The estimated effects of both FRP
671 and AOD exhibit a non-linear, saturating response. LST increases sharply at low-to-moderate
672 values of each predictor but the effect progressively weakens at higher magnitudes,
673 approaching an asymptotic limit. This behaviour likely arises from the complex interplay of
674 radiative and thermodynamic processes associated with biomass-burning emissions. Fire-
675 originated aerosols exert both direct and indirect radiative effects whose magnitudes and
676 signs vary with aerosol loading and composition (Freychet et al., 2019; Xu et al., 2021; Tian et
677 al., 2022). At moderate aerosol loading, UV-absorbing black carbon aerosols may enhance
678 atmospheric heating and can transiently increase near-surface temperature (Jacobson, 2001).
679 Fire-induced convective plumes may initially enhance surface temperatures, whereas strong
680 aerosol build-up can reduce solar transmittance to the ground. Aerosol–cloud interactions
681 further contribute to non-linearity by modifying cloud microphysics, lifetime, and albedo,
682 altering the regional radiative balance. Additionally, aerosol-driven changes in boundary-layer
683 structure, evapotranspiration, and soil moisture introduce additional land-atmosphere

684 feedbacks. Together, these interacting processes operate across multiple spatial and
685 temporal scales and do not scale linearly with aerosol loading or fire intensity, producing the
686 observed non-linear LST response. The RF model therefore provides strong evidence that
687 both fire intensity and fire-derived aerosols exert measurable and non-linear effects on
688 regional LST, with potentially important implications for the regional radiative budget.

689 **3.6 Geographically weighted regression on LST**

690 A Global Moran's I test was first applied to assess spatial autocorrelation in LST across
691 the intensive fire zone for the cumulative five-year period. As shown in Table S6, Moran's I
692 was 0.225, accompanied by a high positive Z-score and a statistically significant p-value (<
693 0.001), indicating a clustered spatial pattern of LST that is highly unlikely (<1%) to have arisen
694 by random chance. Given this spatial dependence, GWR was employed to evaluate spatial
695 heterogeneity in the relationships between LST, FRP, and other predictors. All variables used
696 in the Random Forest model were incorporated into the GWR framework under both pre-
697 defined scenarios. Model specifications and performance metrics including bandwidth and
698 kernel details are mentioned in Table S8.



699
700 Fig. 9. Spatial distribution of FRP and AOD GWR coefficients across intensive fire zone.
701
702 GWR model demonstrated strong explanatory power, with global R^2 values exceeding
0.74, confirming that the selected predictors effectively captured spatial variability in LST. FRP

703 consistently showed a positive and spatially varying association with LST across both
704 scenarios, underscoring its dominant influence in fire-affected regions. Aerosol loading
705 demonstrated weak but spatially heterogeneous effects, reflecting localized differences in
706 aerosol–temperature interactions. Other predictors, including NDVI, RH, AT, PBLH, elevation,
707 and albedo (Fig. S7), exhibited local coefficients ranging from -0.76 to $+0.23$, indicating spatial
708 variability but comparatively weaker contributions to LST modulation across the study area.

709 **Conclusions**

710 The manuscript unfolds by identifying the geospatial variations in crop residue–based
711 fires and their associated impacts on aerosol loading and land surface temperature across
712 northwestern India. Based on year-wise, pixel-level fire intensity, the geographical region with
713 intensive fire activity was initially delineated, and all satellite-derived and reanalysis datasets
714 were subsequently processed exclusively over the selected zone. A robust and consistent
715 spatial correlation between FRP, AOD, and LST was observed across multiple years, indicating
716 potential fire-induced perturbations in LST. The Hurst exponent analysis reaffirmed the long-
717 term persistence of fire intensity, surface temperature, and aerosol loading time series. A
718 grid-based analysis over the intensive fire zone revealed a significant increase in both LST and
719 AOD during the peak fire season.

720 The article further employs the Random Forest model and Geographically weighted
721 regression (GWR) to assess the potential influence of FRP and aerosol loading on LST, while
722 accounting meteorological covariates, physical environment, vegetation characteristic and
723 surface property as confounding factors within the selected zone. Two contrasting scenarios
724 were hypothesized to examine the FRP–LST–AOD nexus. Scenario 1 considered spatially
725 aggregated FRP from fire initiation to subsidence, whereas Scenario 2 focused on days
726 characterized by high-intensity fires exhibiting a strong positive correlation between FRP and
727 LST. In both the scenarios, the Random Forest regression successfully captured and mapped
728 FRP-induced modulation of LST, though with varying magnitudes. A distinct increase in FRP-
729 induced LST modulation was observed during high-intensity fire events. Both boundary layer
730 height and columnar aerosol loading also contributed partially, with aerosols' influence on
731 LST increasing during periods of intense release of fire energy. The Global Moran's I test
732 indicated significant spatial clustering of LST while GWR results further confirmed FRP and

733 AOD-modulated LST variations across northwestern India, highlighting strong spatial
734 heterogeneity in FRP-AOD-LST nexus.

735 This analysis reveals that the biophysical effects of crop residue-based fires across
736 northwestern India can substantially influence the regional radiative budget by altering LST.
737 The magnitude of LST modulation, however, depends on fire intensity and feedbacks from
738 regional meteorology. This study provides novel insights into residue-based fire induced
739 surface temperature dynamics in a region where recurrent fires have been historically linked
740 primarily with deteriorating air quality in Delhi and its surroundings. The observation-driven
741 analysis offers a comprehensive understanding of LST responses to residue burning and helps
742 reduce uncertainties in fire-induced modifications of the radiative budget. Nonetheless,
743 uncertainties remain due to unaccounted agricultural feedbacks, limited temporal coverage,
744 retrieval uncertainty in geospatial datasets, and the complexity in aerosol–meteorology
745 interactions. The multifaced influence of fire aerosols and energy on regional climate through
746 rapid atmospheric and land surface adjustments, remains complicated at the global level. Our
747 findings underscore the need for Earth system model–based simulations to better quantify
748 climate feedbacks from crop residue burning. Besides, assessing the underlying mechanisms
749 of fire-energy-induced changes in evapotranspiration, the radiative effects of aerosols, fire–
750 aerosol–meteorology feedbacks, and incorporating additional proxies could further reduce
751 the uncertainty in estimating radiative impacts from residue burning.

752

753 **Acknowledgments**

754 Authors acknowledges the fund received from Banaras Hindu University under Institute of
755 Eminence grant (6031). Authors also acknowledge open source software like R (V4.4), Python
756 (V3.7) and QGIS (V3.28) for extracting and plotting the dataset.

757 **Data Availability**

758 All the data used in this analysis are available freely. VIIRS and MODIS data can be accessed
759 via NASA Earthdata (<https://earthdata.nasa.gov>), and ERA5 reanalysis data is available from
760 ECMWF Copernicus (<https://cds.climate.copernicus.eu/>). SMAP Soil moisture data is available
761 at https://nsidc.org/data/spl1ctb_e. All dataset were last accessed on November 13, 2025.
762 We thank NASA for providing the VIIRS and MODIS data, and the Copernicus Climate Change
763 Service (C3S) for the ERA5 reanalysis data.

764 **Authors contributions**

765 AP: Data curation, formal analysis and interpretation; RS: Data curation, formal analysis; KA:
766 Data curation, formal analysis; NC: Data curation, formal analysis; TB: conceptualization,
767 methodology and interpretation, funding as well as writing and editing manuscript.

768 **Competing interests.** Authors declare that they have no conflict of interest.

769 **Supporting Information.** The supporting tables (8) and figures (7) are included in
770 supplementary file.

771 **References**

772 Aditi, K., Pandey, A., and Banerjee, T.: Forest fire emission estimates over South Asia using Suomi-NPP
773 VIIRS-based thermal anomalies and emission inventory, *Environ. Pollut.*, 366, 125441,
774 <https://doi.org/10.1016/j.envpol.2025.125441>, 2025.

775 Aditi, K., Singh, A., and Banerjee, T.: Retrieval uncertainty and consistency of Suomi-NPP VIIRS Deep
776 Blue and Dark Target aerosol products under diverse aerosol loading scenarios over South Asia,
777 *Environ. Pollut.*, 331, 121913, <https://doi.org/10.1016/j.envpol.2023.121913>, 2023.

778 Alkama, R., and Cescatti, A.: Biophysical climate impacts of recent changes in global forest cover,
779 *Science*, 351, 600–604, <https://doi.org/10.1126/science.aac8083>, 2016.

780 Andela, N., Morton, D. C., Giglio, L., Chen, Y., van der Werf, G. R., Kasibhatla, P. S., DeFries, R. S., Collatz,
781 G. J., Hantson, S., Kloster, S., Bachelet, D., Forrest, M., Lasslop, G., Li, F., Mangeon, S., Melton, J. R.,
782 Yue, C., and Randerson, J. T.: A human-driven decline in global burned area, *Science*, 356, 1356–1362,
783 <https://doi.org/10.1126/science.aal4108>, 2017.

784 Balwinder-Singh, McDonald, A. J., Srivastava, A. K., Jain, M., and Lobell, D. B.: Trade-offs between
785 groundwater conservation and air pollution from agricultural fires in northwest India, *Nat. Sustain.*, 2,
786 580–583, <https://doi.org/10.1038/s41893-019-0304-4>, 2019.

787 Banerjee, T., Anchule, A., Sorek-Hamer, M., and Latif, M. T.: Vertical stratification of aerosols over
788 South Asian cities, *Environ. Pollut.*, 309, 119776, <https://doi.org/10.1016/j.envpol.2022.119776>, 2022.

789 Banerjee, T., Shitole, A. S., Mhawish, A., Anand, A., Ranjan, R., Khan, M. F., Srithawirat, T., Latif, M. T.,
790 and Mall, R. K.: Aerosol climatology over South and Southeast Asia: Aerosol types, vertical profile, and
791 source fields, *J. Geophys. Res.-Atmos.*, 126, e2020JD033554, <https://doi.org/10.1029/2020JD033554>,
792 2021.

793 Bowman, D. M. J. S., Balch, J. K., Artaxo, P., Bond, W. J., Carlson, J. M., Cochrane, M. A., d'Antonio, C.
794 M., DeFries, R. S., Doyle, J. C., Harrison, S. P., Johnston, F. H., Keeley, J. E., Krawchuk, M. A., Kull, C. A.,
795 Marston, J. B., Moritz, M. A., Prentice, I. C., Roos, C. I., Scott, A. C., Swetnam, T. W., van der Werf, G.
796 R., and Pyne, S. J.: Fire in the Earth system, *Science*, 324, 481–484,
797 <https://doi.org/10.1126/science.1163886>, 2009.

798 Breiman, L.: Random forests, *Mach. Learn.*, 45, 5–32, <https://doi.org/10.1023/A:1010933404324>,
799 2001.

800 Brunsdon, C., Fotheringham, A. S., and Charlton, M. E.: Geographically weighted regression: A method
801 for exploring spatial nonstationarity, *Geogr. Anal.*, 28, 281–298, <https://doi.org/10.1111/j.1538-4632.1996.tb00936.x>, 1996.

803 Brunsdon, C., Fotheringham, S., and Charlton, M.: Geographically weighted regression, *J. Roy. Stat.*
804 *Soc. Ser. D (The Statistician)*, 47, 431–443, <https://doi.org/10.1111/1467-9884.00145>, 1998.

805 Chen, J., Shao, Z., Huang, X., Zhuang, Q., Dang, C., Cai, B., Zheng, X., and Ding, Q.: Assessing the impact
806 of drought–land cover change on global vegetation greenness and productivity, *Sci. Total Environ.*,
807 852, 158499, <https://doi.org/10.1016/j.scitotenv.2022.158499>, 2022.

808 Chuvieco, E., Pettinari, M. L., Koutsias, N., Forkel, M., Hantson, S., and Turco, M.: Human and climate
809 drivers of global biomass burning variability, *Sci. Total Environ.*, 779, 146361,
810 <https://doi.org/10.1016/j.scitotenv.2021.146361>, 2021.

811 Copernicus Climate Change Service: Agrometeorological indicators from 1979 to present derived from
812 reanalysis, Copernicus Climate Change Service (C3S) Climate Data Store (CDS),
813 <https://doi.org/10.24381/cds.6c68c9bb>, accessed: 25 February 2025, 2020.

814 Daoud, J. I.: Multicollinearity and regression analysis, *J. Phys. Conf. Ser.*, 949, 012009,
815 <https://doi.org/10.1088/1742-6596/949/1/012009>, 2017.

816 Fotheringham, A. S., Brunsdon, C., and Charlton, M.: Geographically weighted regression, in: *The SAGE*
817 *Handbook of Spatial Analysis*, SAGE Publications, London, 243–254, 2009.

818 Freychet, N., Tett, S. F. B., Bollasina, M., Wang, K. C., & Hegerl, G.: The local aerosol emission effect on
819 surface shortwave radiation and temperatures. *Journal of Advances in Modeling Earth Systems*, 11,
820 806–817. <https://doi.org/10.1029/2018MS001530>, 2019.

821 Frazier, P. I.: A tutorial on Bayesian optimization. *arXiv preprint arXiv:1807.02811*, 2018.

822 Giglio, L., Descloitres, J., Justice, C. O., and Kaufman, Y. J.: An enhanced contextual fire detection
823 algorithm for MODIS, *Remote Sens. Environ.*, 87, 273–282, [https://doi.org/10.1016/S0034-4257\(03\)00184-6](https://doi.org/10.1016/S0034-4257(03)00184-6), 2003.

825 Gomez, J. L., Allen, R. J., and Li, K. F.: California wildfire smoke contributes to a positive atmospheric
826 temperature anomaly over the western United States, *Atmos. Chem. Phys.*, 24, 6937–6963,
827 <https://doi.org/10.5194/acp-24-6937-2024>, 2024.

828 Graham, M. H.: Confronting multicollinearity in ecological multiple regression, *Ecology*, 84, 2809–
829 2815, <https://doi.org/10.1890/02-3114>, 2003.

830 Granero, M. S., Segovia, J. T., and Pérez, J. G.: Some comments on Hurst exponent and the long
831 memory processes on capital markets, *Physica A*, 387, 5543–5551,
832 <https://doi.org/10.1016/j.physa.2008.05.064>, 2008.

833 Graham, M. H., Haynes, R. J., and Meyer, J. H.: Soil organic matter content and quality: Effects of
834 fertilizer applications, burning, and trash retention on a long-term sugarcane experiment in South
835 Africa, *Soil Biol. Biochem.*, 34, 93–102, [https://doi.org/10.1016/S0038-0717\(01\)00162-2](https://doi.org/10.1016/S0038-0717(01)00162-2), 2002.

836 Hurst, H. E.: Long term storage capacity of reservoirs, *Trans. Am. Soc. Civ. Eng.*, 6, 770–799, 1951.

837 Hsu, N. C., Herman, J. R., and Tsay, S. C.: Radiative impacts from biomass burning in the presence of
838 clouds during boreal spring in Southeast Asia, *Geophys. Res. Lett.*, 30, 1234,
839 <https://doi.org/10.1029/2002GL016485>, 2003.

840 Ichoku, C., Giglio, L., Wooster, M. J., and Remer, L. A.: Global characterization of biomass-burning
841 patterns using satellite measurements of fire radiative energy, *Remote Sens. Environ.*, 112, 2950–
842 2962, <https://doi.org/10.1016/j.rse.2008.02.009>, 2008.

843 Jacobson, M. Z.: Strong radiative heating due to the mixing state of black carbon in atmospheric
844 aerosols, *Nature*, 409, 695–697, <https://doi.org/10.1038/35055518>, 2001.

845 Jethva, H., Torres, O., Field, R. D., Lyapustin, A., Gautam, R., and Kayetha, V.: Connecting crop
846 productivity, residue fires, and air quality over northern India, *Sci. Rep.*, 9, 16594,
847 <https://doi.org/10.1038/s41598-019-52799-x>, 2019.

848 Kant, S., Sarangi, C., and Wilcox, E. M.: Aerosol processes perturb cloud trends over Bay of Bengal:
849 Observational evidence, *npj Clim. Atmos. Sci.*, 6, 132, <https://doi.org/10.1038/s41612-023-00442-5>,
850 2023.

851 Korontzi, S., McCarty, J., Loboda, T., Kumar, S., and Justice, C. O.: Global distribution of agricultural
852 fires in croplands from 3 years of Moderate Resolution Imaging Spectroradiometer (MODIS) data,
853 *Glob. Biogeochem. Cycles*, 20, GB2021, <https://doi.org/10.1029/2005GB002529>, 2006.

854 Lasko, K., and Vadrevu, K.: Improved rice residue burning emissions estimates: Accounting for
855 practice-specific emission factors in air pollution assessments of Vietnam, *Environ. Pollut.*, 236, 795–
856 806, <https://doi.org/10.1016/j.envpol.2018.01.114>, 2018.

857 Li, F., Zhang, X., Kondragunta, S., and Csiszar, I.: Comparison of fire radiative power estimates from
858 VIIRS and MODIS observations, *J. Geophys. Res.-Atmos.*, 123, 4545–4563,
859 <https://doi.org/10.1029/2017JD027823>, 2018.

860 Li, Z. L., Wu, H., Duan, S. B., Zhao, W., Ren, H., Liu, X., Leng, P., Tang, R., Ye, X., Zhu, J., and Sun, Y.:
861 Satellite remote sensing of global land surface temperature: Definition, methods, products, and
862 applications, *Rev. Geophys.*, 61, e2022RG000780, <https://doi.org/10.1029/2022RG000780>, 2023.

863 Liu, Z., Ballantyne, A. P., and Cooper, L. A.: Increases in land surface temperature in response to fire in
864 Siberian boreal forests and their attribution to biophysical processes, *Geophys. Res. Lett.*, 45, 6485–
865 6494, <https://doi.org/10.1029/2018GL078283>, 2018.

866 Liu, Z., Ballantyne, A. P., and Cooper, L. A.: Biophysical feedback of global forest fires on surface
867 temperature, *Nat. Commun.*, 10, 214, <https://doi.org/10.1038/s41467-018-08237-z>, 2019.

868 Logan, T. M., Zaitchik, B., Guikema, S., and Nisbet, A.: Night and day: The influence and relative
869 importance of urban characteristics on remotely sensed land surface temperature, *Remote Sens. Environ.*, 247, 111861, <https://doi.org/10.1016/j.rse.2020.111861>, 2020.

871 Lan, R., Eastham, S. D., Liu, T., Norford, L. K., and Barrett, S. R. H.: Air quality impacts of crop residue
872 burning in India and mitigation alternatives, *Nat. Commun.*, 13, 6537,
873 <https://doi.org/10.1038/s41467-022-34284-6>, 2022.

874 Markonis, Y., and Koutsoyiannis, D.: Scale-dependence of persistence in precipitation records, *Nat. Clim. Change*, 6, 399–401, <https://doi.org/10.1038/nclimate2894>, 2016.

876 Mhawish, A., Sarangi, C., Babu, P., Kumar, M., Bilal, M., and Qiu, Z.: Observational evidence of elevated
877 smoke layers during crop residue burning season over Delhi: Potential implications on associated
878 heterogeneous PM_{2.5} enhancements, *Remote Sens. Environ.*, 280, 113167,
879 <https://doi.org/10.1016/j.rse.2022.113167>, 2022.

880 NAAS (National Academy of Agricultural Sciences): Innovative viable solution to rice residue burning
881 in rice–wheat cropping system through concurrent use of Super Straw Management System-fitted
882 combines and Turbo Happy Seeder, National Academy of Agricultural Sciences, New Delhi, India, 2017.

883 Nguyen, H. M., and Wooster, M. J.: Advances in the estimation of high spatio-temporal resolution pan-
884 African top-down biomass burning emissions made using geostationary fire radiative power (FRP) and
885 MAIAC aerosol optical depth (AOD) data, *Remote Sens. Environ.*, 248, 111971,
886 <https://doi.org/10.1016/j.rse.2020.111971>, 2020.

887 Prasad, A. K., Singh, R. P., and Kafatos, M.: Influence of coal-based thermal power plants on aerosol
888 optical properties in the Indo-Gangetic Basin, *Geophys. Res. Lett.*, 33, L05805,
889 <https://doi.org/10.1029/2005GL023801>, 2006.

890 Puissant, A., Rougier, S., & Stumpf, A.: Object-oriented mapping of urban trees using Random
891 Forest classifiers. *Int. J. Appl. Earth Obs. Geoinf.*, 26, 235–245.
892 <https://doi.org/10.1016/j.jag.2013.07.002>, 2014.

893 Ramanathan, V., and Carmichael, G.: Global and regional climate changes due to black carbon, *Nat.*
894 *Geosci.*, 1, 221–227, <https://doi.org/10.1038/ngeo156>, 2008.

895 Ramana, M. V., Ramanathan, V., Podgorny, I. A., Pradhan, B. B., and Shrestha, B.: The direct
896 observations of large aerosol radiative forcing due to black carbon in the Himalayan region, *Geophys.*
897 *Res. Lett.*, 31, L05111, <https://doi.org/10.1029/2003GL018824>, 2004.

898 Remer, L. A., Kaufman, Y. J., Tanré, D., Mattoo, S., Chu, D. A., Martins, J. V., Li, R. R., Ichoku, C., Levy,
899 R. C., Kleidman, R. G., Eck, T. F., Vermote, E., and Holben, B. N.: The MODIS aerosol algorithm,
900 products, and validation, *J. Atmos. Sci.*, 62, 947–973, <https://doi.org/10.1175/JAS3385.1>, 2005.

901 Sayer, A. M., Hsu, N. C., Bettenhausen, C., and Jeong, M. J.: Validation and uncertainty estimates for
902 MODIS Collection 6 “Deep Blue” aerosol data, *J. Geophys. Res.-Atmos.*, 118, 7864–7872,
903 <https://doi.org/10.1002/jgrd.50600>, 2013.

904 Schroeder, W., Oliva, P., Giglio, L., and Csiszar, I. A.: The new VIIRS 375 m active fire detection data
905 product: Algorithm description and initial assessment, *Remote Sens. Environ.*, 143, 85–96,
906 <https://doi.org/10.1016/j.rse.2013.12.008>, 2014.

907 Seinfeld, J. H., and Pandis, S. N.: *Atmospheric Chemistry and Physics: From Air Pollution to Climate
908 Change*, John Wiley & Sons, Hoboken, New Jersey, 2016.

909 Sharma, N., Kaskaoutis, D. G., Singh, R. P., and Singh, S.: Impact of two intense dust storms and
910 associated mixing with biomass burning aerosols over the Indo-Gangetic Basin, *Atmos. Environ.*, 138,
911 167–180, <https://doi.org/10.1016/j.atmosenv.2016.05.002>, 2016.

912 Shahriari, B., Swersky, K., Wang, Z., Adams, R. P., & De Freitas, N.: Taking the human out of the loop:
913 A review of Bayesian optimization. *Proceedings of the IEEE*, 104(1), 148–175, 2015.

914 Shikwambana, L., and Mhangara, P.: Characterization of biomass burning aerosol over southern Africa
915 using multiple satellite data, *Int. J. Remote Sens.*, 39, 4764–4780,
916 <https://doi.org/10.1080/01431161.2018.1448481>, 2018.

917 Shikwambana, L., and Mhangara, P.: Analysis of the impact of biomass burning on tropospheric NO₂
918 over southern Africa during 2018, *Environ. Pollut.*, 261, 114204,
919 <https://doi.org/10.1016/j.envpol.2020.114204>, 2020.

920 Shikwambana, L., and Kganyago, M.: The contribution of biomass burning to carbon monoxide
921 concentrations in southern Africa: A case study of 2019, *Atmosphere*, 12, 878,
922 <https://doi.org/10.3390/atmos12070878>, 2021.

923 Singh, R. P., and Kaskaoutis, D. G.: Crop residue burning: A threat to South Asian air quality, *Eos Trans.
924 AGU*, 95, 333–334, <https://doi.org/10.1002/2014EO370001>, 2014.

925 Song, C. H., and Carmichael, G. R.: A three-dimensional modeling investigation of the evolution
926 processes of dust and carbonaceous aerosols over East Asia, *J. Geophys. Res.-Atmos.*, 106, 18131–
927 18154, <https://doi.org/10.1029/2000JD900511>, 2001.

928 Snoek, J., Larochelle, H., and Adams, R.P.: Practical bayesian optimization of machine learning
929 algorithms. *Advances in neural information processing systems*, 25, 2012.

930 Srivastava, A. K., Singh, S., Pant, P., Dumka, U. C., and Holben, B. N.: Black carbon aerosols over Manora
931 Peak in the Indian Himalayan foothills: Implications for climate forcing, *Environ. Res. Lett.*, 7, 014002,
932 <https://doi.org/10.1088/1748-9326/7/1/014002>, 2012.

933 Stein, A. F., Draxler, R. R., Rolph, G. D., Stunder, B. J. B., Cohen, M. D., and Ngan, F.: NOAA's HYSPLIT
934 atmospheric transport and dispersion modeling system, *Bull. Am. Meteorol. Soc.*, 96, 2059–2077,
935 <https://doi.org/10.1175/BAMS-D-14-00110.1>, 2015.

936 Tiwari, S., Singh, A. K., Singh, S., and Pervez, S.: Aerosol climatology over Varanasi using MODIS and
937 MISR satellite data, *Air Qual. Atmos. Health*, 8, 301–309, <https://doi.org/10.1007/s11869-014-0285-8>, 2015.

939 Tian, C., Yue, X., Zhu, J., Liao, H., Yang, Y., Lei, Y., Zhou, X., Zhou, H., Ma, Y., and Cao, Y.: Fire–climate
940 interactions through the aerosol radiative effect in a global chemistry–climate–vegetation model,
941 *Atmos. Chem. Phys.*, 22, 12353–12366, <https://doi.org/10.5194/acp-22-12353-2022>, 2022.

942 Vadrevu, K. P., Ellicott, E. A., Giglio, L., Badarinath, K. V. S., Vermote, E., Justice, C., and Lau, W. K. M.:
943 Vegetation fires in the Himalayan region – Aerosol load, black carbon emissions and climate forcing,
944 *Remote Sens. Environ.*, 123, 324–334, <https://doi.org/10.1016/j.rse.2012.03.021>, 2012.

945 van der Werf, G. R., Randerson, J. T., Giglio, L., van Leeuwen, T. T., Chen, Y., Rogers, B. M., Mu, M., van
946 Marle, M. J. E., Morton, D. C., Collatz, G. J., Yokelson, R. J., and Kasibhatla, P. S.: Global fire emissions
947 estimates during 1997–2016, *Earth Syst. Sci. Data*, 9, 697–720, <https://doi.org/10.5194/essd-9-697-2017>, 2017.

949 Vadrevu, K. P., Lasko, K., Giglio, L., and Justice, C.: Analysis of Southeast Asian pollution episode using
950 satellite remote sensing data, *Atmos. Environ.*, 125, 512–522,
951 <https://doi.org/10.1016/j.atmosenv.2015.11.032>, 2016.

952 Vinjamuri, K.S., Mhawish, A., Banerjee, T., Sorek-Hamer, M., Broday, D.M., Mall, R.K. and Latif, M.T.:
953 Vertical distribution of smoke aerosols over upper Indo-Gangetic Plain. *Environmental pollution*, 257,
954 p.113377, 2020.

955 Wang, J., Christopher, S. A., Nair, U. S., Reid, J. S., Prins, E. M., Szykman, J., and Hand, J. L.: Mesoscale
956 modeling of Central American smoke transport to the United States: 1. “Top-down” assessment of
957 emission strength and diurnal variation impacts, *J. Geophys. Res.-Atmos.*, 111, D05S17,
958 <https://doi.org/10.1029/2005JD006416>, 2006.

959 Xu, L., Zhu, Q., Riley, W. J., Chen, Y., Wang, H., Ma, P.-L., and Randerson, J. T.: The Influence of Fire
960 Aerosols on Surface Climate and Gross Primary Production in the Energy Exascale Earth System Model
961 (E3SM), *J. Climate*, 34, 7219–7238, <https://doi.org/10.1175/JCLI-D-21-0193.1>, 2021.

962 Yang, J., and Zhao, Y.: Impacts of forest fires on surface temperature and precipitation in boreal
963 regions: An observational analysis, *Environ. Res. Lett.*, 15, 124046, <https://doi.org/10.1088/1748-9326/abc123>, 2020.

965 Zhao, T., Li, J., and Zhang, W.: Long-term changes in land surface temperature associated with
966 agricultural burning in eastern China, *Remote Sens.*, 13, 1215, <https://doi.org/10.3390/rs13061215>,
967 2021.

968